

Two-dimensional Dirac semimetal based on the alkaline earth metal CaP_3

Seoung-Hun Kang

Materials Science and Technology Division, Oak Ridge National Laboratory, Oak Ridge, Tennessee 37831, USA


Wei Luo

Center for Nanophase Materials Sciences, Oak Ridge National Laboratory, Oak Ridge, Tennessee 37831, USA

Sinchul Yeom

Materials Science and Technology Division, Oak Ridge National Laboratory, Oak Ridge, Tennessee 37831, USA

Yaling Zheng

*Department of Physics and Astronomy, University of Tennessee, Knoxville, Tennessee 37996, USA*Mina Yoon **Materials Science and Technology Division, Oak Ridge National Laboratory, Oak Ridge, Tennessee 37831, USA* (Received 2 March 2023; revised 6 September 2023; accepted 3 October 2023; published 14 December 2023)

Using an evolutionary algorithm in combination with first-principles density-functional theory calculations, we identify a two-dimensional (2D) CaP_3 monolayer as a new Dirac semimetal due to inversion and nonsymmorphic spatial symmetries of the structure. This new topological material, composed of light elements, exhibits high structural stability (higher than the phase known in the literature), which is confirmed by thermodynamic and kinetic stability analysis. Moreover, it satisfies the electron filling criteria, so that its Dirac state is located near the Fermi level. The existence of the Dirac state predicted by the theoretical symmetry analysis is also confirmed by first-principles electronic band structure calculations. We find that the energy position of the Dirac state can be tuned by strain, while the Dirac state is unstable against an external electric field since it breaks the spatial inversion symmetry. Our findings should be instrumental in the development of 2D Dirac fermions based on light elements for their application in nanoelectronic devices and topological electronics.

DOI: [10.1103/PhysRevMaterials.7.124202](https://doi.org/10.1103/PhysRevMaterials.7.124202)**I. INTRODUCTION**

Electronic band structures are fingerprints of the crystal symmetry of solids [1], determining their band degeneracies and band topologies. The crystal symmetry becomes more prominent in accommodating the Dirac state in low-dimensional systems, such as two-dimensional (2D) atomic thick material like graphene [2]. As the Dirac state in the graphene is guaranteed by crystal symmetry, spin-orbit coupling (SOC) breaks the Dirac state. Resulting in a small band gap [3,4], graphene becomes a topological insulator [5]. Many other 2D materials such as silicene [6,7], germanene [6,8], 2D boron and carbon allotropes [9–14], group-VA phosphorus structures [15–17], and 5d transition metal trichloride [18] have similar properties to graphene.

Theoretical studies have so far predicted many 2D topological states [17,19–21]. Among the states of fundamental interest are those protected by the interplay of different symmetries. For example, a 2D Dirac state is predicted to be guaranteed if the system with nonsymmorphic space group maintains both inversion and time-reversal symmetries (TRS) [22]. Another interesting state is the 2D Dirac state for a

system with two nonsymmorphic space group symmetries, where the Dirac state is at the time-reversal invariant momenta (TRIMs) [17]. One of the challenges in the field is to bring the Dirac states close to the Fermi level (E_F) so that the topologically protected state can be observed and used in experiments. In the pristine structure, the location of the Dirac state is primarily determined by the electron filling [22,23]. Many of the 2D materials that stabilize the Dirac state do not satisfy the partial filling state of the electrons, so their energy levels are far from the E_F [16,17,24]. While the position of the Fermi level can be controlled by mechanical strain [25] or chemical doping [26], finding the desirable electronic properties of thermodynamically stable structures could be another challenge.

Recently, there has been interest in a new family of theoretically proposed materials with high mobility [27], good thermoelectrics [28], and defect properties [29]. In particular, in the five years, since the prediction of a stable 2D CaP_3 phase, its existence has not been experimentally confirmed. It is necessary to study the possibility of synthesizing this material and its stability.

In this paper, we report a new 2D Dirac semimetal as a result of inversion and nonsymmorphic spatial symmetries of the structure. It is a new phase of 2D CaP_3 with the Dirac state near the Fermi level. The structure is discovered

*myoon@ornl.gov

by performing first-principles calculations combined with an evolutionary algorithm. Our motivation for exploring the AB_3 family of materials was to focus on the 1 and 5 groups among the combinations of elements in the periodic table that satisfy the aforementioned electron filling condition ($4n + 2$) and Dirac states by nonsymmorphic and inversion symmetry, which are two-dimensional and preferably composed of light elements. Theoretical symmetry analysis agrees well with the first-principles band structures and proves the existence of two Dirac states protected by inversion and nonsymmorphic space symmetries at TRIMs in the Brillouin zone (BZ) boundary. The new structure proves to be dynamically and thermodynamically stable, as indicated by our phonon analysis and molecular dynamics (MD) simulations at high temperatures (500 K). In addition, we investigate the stability of the Dirac state by applying various symmetric lattice strains, such as biaxial, uniaxial, and shear strains, and confirm that the properties of the Dirac state are intact under these strains, but only its position in momentum space changes. Therefore, we propose strain as an effective method to tune the location of the Dirac state. Our results demonstrate how crystal symmetry plays a role in stabilizing Dirac states in 2D materials and the influence of external parameters to tune the electronic properties to the desirable outcome.

II. CALCULATIONAL APPROACHES

To identify thermodynamically stable structures of 2D CaP_3 , we perform crystal prediction calculations using the particle swarm optimization (PSO) algorithm implemented in Crystal Structure Analysis by Particle Swarm Optimization (CALYPSO) [30,31]. At the beginning of the simulation, we start with 20 random structures within 2D space groups, and the structural evolution proceeds up to six generations based on the PSO scheme. At the end of the simulation, 111 2D configurations are identified, all containing a 60 \AA vacuum layer. The total energies of the configurations are calculated using the all-electron full-potential FHI-aims code [32–34] with the Perdew-Burke-Ernzerhof (PBE) exchange-correlation functional [35]. The tight numerical settings and $4 \times 4 \times 1$ k -point grids are used in these calculations. All structures are fully optimized using the Broyden-Fletcher-Goldfarb-Shanno (BFGS) [36] algorithm, with a maximum force component below 10^{-3} eV/\AA .

For their structural, electronic, and vibrational properties, we carried out first-principles calculations based on density-functional theory (DFT) using Vienna *ab initio* simulation package (VASP) [37,38]. Projector-augmented wave potentials [39] were employed to describe the interaction between ions and valence electrons. The generalized gradient approximation (GGA) of PBE [35] was used as the exchange-correlation functional. The cutoff energy for the plane wave basis was chosen to be 400 eV. The Brillouin zone (BZ) was sampled using Γ -centered $8 \times 8 \times 1$ grid. To avoid the spurious interlayer interaction, we introduced a vacuum region of 20 \AA along the c axis perpendicular to the sheet. Atomic relaxations were done until the Hellmann-Feynman force acting on every atom became smaller than 0.01 eV/\AA . SOC is considered for all calculations. The vibrational property of CaP_3 was evaluated using the harmonic approximation implemented in

the PHONOPY package [40]. We used $3 \times 3 \times 1$ supercell structures for the optimized structure of CaP_3 . The dynamics were studied via canonical *ab initio* molecular dynamics (MD) simulations with 1 fs time steps. To confirm the stability at a higher temperature than room temperature, we used 500 K for 7 ps to reach thermal equilibrium with a $4 \times 4 \times 1$ supercell (128 atoms).

III. RESULTS AND DISCUSSION

The evolutionary algorithm based on the first-principles DFT calculations identified various stable crystal structures of CaP_3 . Among them, we compiled the first 50 most stable structures in the structural frequencies in Fig. 1(a) and the energy distributions of the polymorphs in Fig. 1(b). The most stable phase found in our study is a $\approx 1 \text{ eV}$ band-gap semiconductor with $P\bar{1}$ symmetry, and the second most stable phase is also a $\approx 1 \text{ eV}$ band-gap semiconductor with $C2$ symmetry with energy higher by 35 meV/atom (for their atomic structures and band structure, see Supplemental Material [41]). We confirm that these two lowest structures have no interesting topological features. The next stable structure has $P2/c$ symmetry with an energy 25 meV/atom higher than the $C2$ structure, but it is even more stable than the previously reported $P\bar{1}(2)$ phase with 75 meV/atom [27]. Among these phases, we found the $P2/c$ phase to be the most interesting—crystal symmetry exhibits both inversion and nonsymmorphic symmetries. From now on, we focus on the $P2/c$ phase and refer to it as the CaP_3 unless otherwise stated. The CaP_3 consists of a distorted hexagonal unit cell with an angle of $\approx 45^\circ$ between the cell vectors as shown in Fig. 1(c). Figure 1(d) analyzes the crystal symmetries, where the orange star is an inversion center for the symmetry operation (indicated by the red arrows), and the blue arrows indicate a nonsymmorphic symmetry consisting of mirror operation of the xy plane with half translation along the x axis (for the optimized atomic positions, see Supplemental Material [41]).

Next, we investigate the electronic properties of CaP_3 . Figures 2(a) and 2(b) show the electronic band structures and the Fermi surface of CaP_3 with SOC along the high-symmetry line in BZ as shown in Fig. 2(b). The CaP_3 exhibits a metallic state with two bands crossing at the X and M points near the Fermi level. The presence of both inversion (P) and time-reversal (Θ) symmetries guarantees the twofold degenerate band with SOC at all BZ. Therefore, the crossing points at the X and M points are the locations where the fourfold degenerated Dirac state exists. The band structure also represents a small SOC effect for light elements and yields essentially the same eigenvalues regardless of SOC.

We then perform a symmetry analysis to explain the protection of the Dirac points at the X and M points. In the following analysis, we include the electron spin and the SOC. The crystal symmetries underlying the CaP_3 , characterized by the inversion (P) and nonsymmorphic (\tilde{M}_z) operations, can be decomposed into products of point and translation group operations as $\tilde{M}_z = M_z T_{a\hat{x}/2}$ [22]. Here, M_z is the mirror operation about the xy plane and $T_{a\hat{x}/2}$ is the translation by half translation along the x axis, as shown in Fig. 1(d). For the nonsymmorphic symmetry, the point-group operator should commute with the translation-group operation. The represen-

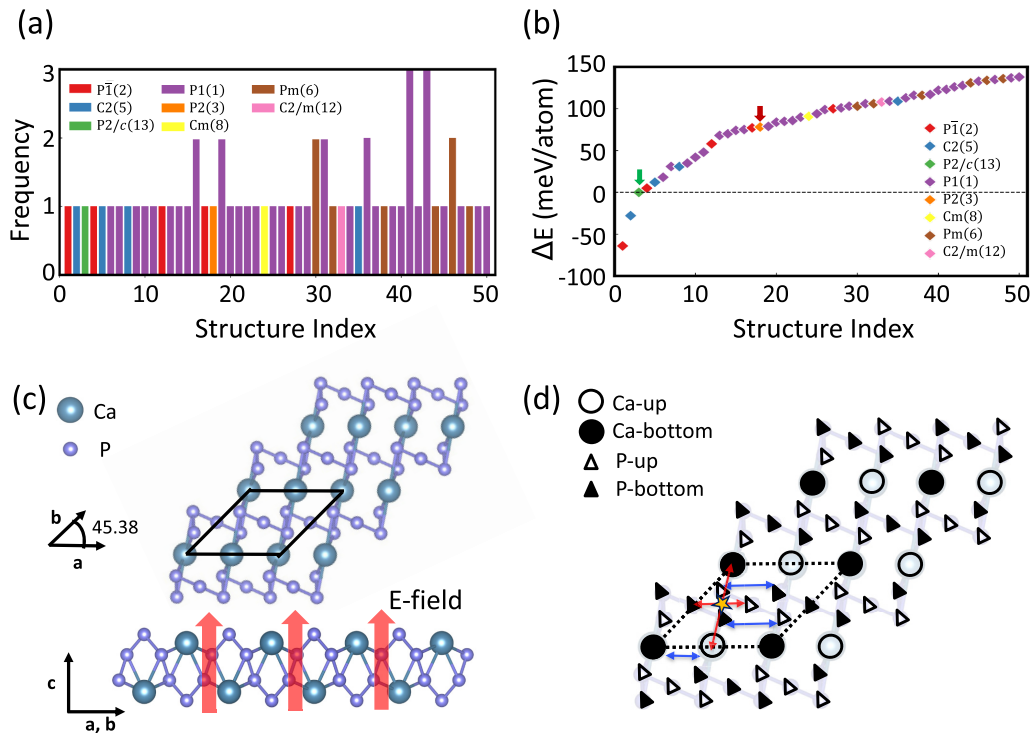


FIG. 1. Stable configurations and crystal structures of topological CaP₃ (*P2/c*). (a) The low-energy structures of 2D CaP₃ are found by the PSO algorithm. The crystal structures are color coded and ordered according to the energy hierarchy, i.e., the first one is the most stable structure. The y axis represents the number of occurrences of a structure with the same energy and a space group. The CaP₃ with *P2/c* symmetry is the topological Dirac semimetal identified in this study. (b) The energy (ΔE) of the polymorphs with respect to the *P2/c* structure (green arrow), with the red arrow indicating the previously reported structure [27]. The CaP₃ with *P $\bar{1}$* and *C2* is more stable for *P2/c*, the structure of this study. (c) Top and side views of the *P2/c* structure representing a distorted hexagonal lattice (highlighted by the unit cell of the black line). (d) The circles and triangles represent Ca and P atoms, respectively, with the solids and hollows representing below and above the mirror plane (M_z) on the xy plane, respectively. The orange star is the inversion point, and the red and blue arrows denote atoms corresponding to the inversion and asymmetric symmetry of certain atoms in the unit cell.

tation of $T_{a\hat{x}/2}$ for a Bloch state with k_x is $T_{a\hat{x}/2} = e^{ik_x a/2}$, that is, \tilde{M}_z becomes $\tilde{M}_z = M_z e^{ik_x a/2}$. To find the eigenvalues of \tilde{M}_z , we note that

$$(\tilde{M}_z)^2 = M_z^2 e^{ik_x a} = -e^{ik_x a},$$

where $e^{ik_x a}$ denotes the translation by one unit cell along x directions and M_z^2 is -1 from the 2π rotation on spin. The spinor representation of M_z is given by $M_z = i\sigma_z \otimes R_z(\pi)P$, where σ_z is the z component of the Pauli spin matrices affecting only the spin parts of the wavefunction; $R_z(\pi)$ and P are, respectively, a real space rotation around the z axis by an angle π and an inversion $\mathbf{r} \rightarrow -\mathbf{r}$ affecting only the orbital parts of the wavefunction. We use that the mirror operation is a multiple of two operations, an inversion followed by a π rotation, and that the representation of an inversion in the spin-half space is the identity. The eigenvalues resulting from the solution of $\tilde{M}_z \psi = E_z \psi$ are $E_z = \pm i e^{ik_x a/2}$. Now, we consider the inversion symmetry (P) operation with the nonsymmorphic (\tilde{M}_z) symmetry. These operations, represented as $\tilde{M}_z : (x, y, z) \rightarrow (x + 1/2, y, -z)$ and $P : (x, y, z) \rightarrow (-x, -y, -z)$, do not commute each other. For the time-reversal symmetry operation with $\tilde{M}_z P_z P \tilde{M}_z$ holds $\tilde{M}_z P \Theta : (x, y, z) \rightarrow (-x + 1/2, -y, z)$ and $P \Theta \tilde{M}_z : (x, y, z) \rightarrow (-x - 1/2, -y, z)$, respectively. Therefore, $\tilde{M}_z P = e^{ik_x a} P \tilde{M}_z$ and $\tilde{M}_z P \Theta = e^{ik_x a} P \Theta \tilde{M}_z$ and, for

an eigenstate $|E_z\rangle$ of with eigenvalue E_z , it becomes $\tilde{M}_z(P\Theta|E_z\rangle) = e^{ik_x a} \pm i e^{ik_x a/2}(P\Theta|E_z\rangle) = -E_z(P\Theta|E_z\rangle)$. Due to P and Θ symmetries under SOC, all bands are twofold degenerate with $|E_z\rangle$ and $P\Theta|E_z\rangle$ at the whole k points. For $k_x = \pi/a$, E_z is ± 1 and the $[\tilde{M}_z, P]$ is 0. Two space group (symmetric) operators that anticommute guarantee twofold degeneracy [23]. Moreover, X and M points are TRIM points, therefore all states $|E_z\rangle$ at the X point have another degenerate Kramer's pair $\Theta|E_z\rangle$ with the same eigenvalue E_z . The four eigenstates such as $|E_z\rangle$, $\Theta|E_z\rangle$, $P\Theta|E_z\rangle$, and $P|E_z\rangle$, are degenerate at X and M points. Except for the TRIM points, X, Y, and M points, it is not invariant with the Θ operation, so the fourfold degeneracy is broken by two doubly degenerate bands. For the Y point, $k_x = 0$ and $k_y = \pi/a$, the anticommute for \tilde{M}_z and P is not satisfied, so it has only a twofold degeneracy for the inversion symmetry.

Our symmetry analysis predicts the fourfold degenerate Dirac states at the X and M points. To verify the theoretical prediction, we perform first-principles calculations of the band structures. In particular, we break the inversion symmetry of the CaP₃ by applying an electric field perpendicular to the surface in Fig. 1(c). In principle, any field strength breaks the symmetry, leading to the splitting of degenerate states if present. In practice, however, the splitting is difficult to detect if the field strength is too low. Therefore, we choose

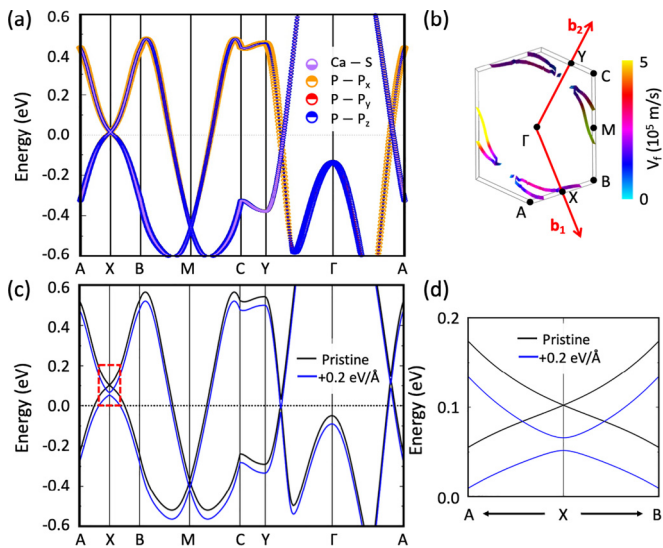


FIG. 2. Electronic structure of CaP_3 . (a) Orbital-projected band structure featuring the Ca- s and P- p orbitals for pristine CaP_3 . (b) The color-coordinated Fermi surface represents the Fermi velocity of the bands, and the Brillouin zone illustrates the band paths along the high-symmetry points. (c) Electronic energy bands of the pristine CaP_3 (black line) compared to those with a $+0.2 \text{ eV/\AA}$ electric field applied perpendicular to the surface (blue line). (d) The inset corresponds to the red dotted rectangle in (c).

a large field strength, $+0.2 \text{ eV/\AA}$, as an example. Figure 2(a) compares the changes in the band structures due to the electric field. The E field indeed breaks the inversion symmetry, leading to the splitting of two doubly degenerate bands in the X and M points, which are protected by the time-reversal symmetry. Figures 2(c) and 2(d) compare the changes in the band structures due to the electric field. The E field indeed breaks the inversion symmetry, leading to the splitting of two doubly degenerate bands in the X and M points, which are protected by the time-reversal symmetry. These results also show the band structures of CaP_3 with full BZ and the other alkaline earth metal trinitogenide such as SrP_3 and BaP_3 (see Supplemental Material [41]).

The number of electrons of CaP_3 satisfies the electron filling condition ($4n + 2, n = 11$) [22,23], leading to the Dirac states near the Fermi level: $+100 \text{ meV}$ and -400 meV at X and M points, respectively. To move the Dirac state closer to the Fermi level, some external perturbations are required, such as the application of an E field. However, the electric field is not ideal since it breaks the spatial inversion symmetry. Therefore, we focus on the strain to preserve the crystal symmetry as shown in Fig. 3. Since the Dirac state of CaP_3 is guaranteed by the inversion symmetry, the time-reversal symmetry, and the nonsymmorphic symmetry, the Dirac state cannot be broken if these symmetries are preserved. In Fig. 3(a), we first estimate the energy costs for different strains. The application of strains up to about $+5\%$ increases the energy by 30 meV , which corresponds to a thermal energy variation of 300 K . Therefore, we assume that these structures are stable at room temperature. The energy levels of the Dirac states at the X and M points can be tuned by stretching as shown in Figs. 3(b)

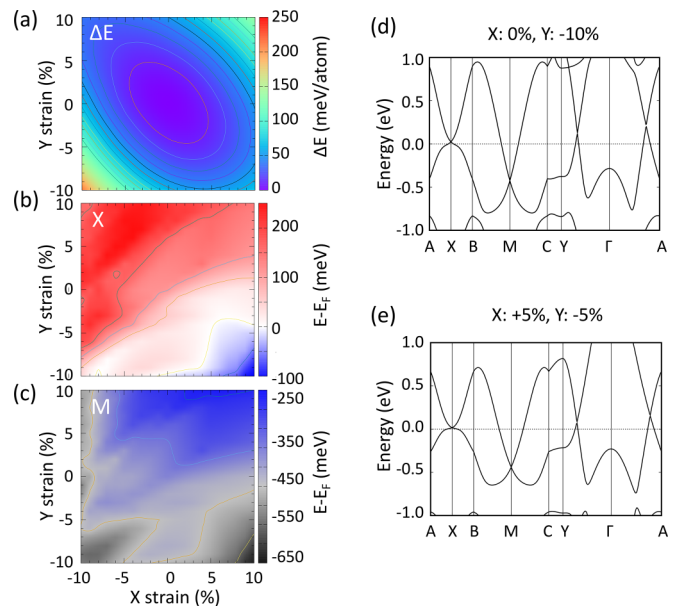


FIG. 3. The effects of strains on the stability and electronic properties of CaP_3 . (a) Changes in the total energy (eV/atom) of the structure by applying strains, where the energy is given with respect to the equilibrium structure. (b), (c) The energy level of the Dirac state with respect to the Fermi level as a function of the strains at X and M points, respectively. (d), (e) Band structures with uniaxial compressive strain (X:0%, Y:-10%) and biaxial strain (X:+5%, Y:-5%), respectively.

and 3(c). We find that the energy level of the Dirac state of the X point is mobile and can find the Fermi level by strain, whereas the energy level of the M point remains more than 250 meV below the Fermi level regardless of strain. The Dirac state of the X point is pinned to the E_F at certain strains, such as 10% compressive strain in the y direction and 5% tensile strain in the x direction with 5% compressive strain in the y direction in Fig. 3(b). In Figs. 3(d) and 3(e), it is confirmed that the Dirac state is pinned to the E_F ; the symmetries protecting the Dirac state are robust against various strains, such as biaxial, uniaxial, and shear deformation in the plane.

Regardless of the cohesive energy, a structure can be considered stable only if it does not change spontaneously. The spontaneous structural change can be due to a negative frequency in the vibrational band dispersion. To verify the stability and structural rigidity for CaP_3 , we investigate the vibration spectra of its structure as presented in Fig. 4(a). The absence of a negative frequency in the phonon band means that CaP_3 is dynamically stable. Since the slope of the longitudinal acoustic (LA) branch near the Γ is isotropic, the rigidity in the $\Gamma - \text{M}$ direction and the $\Gamma - \text{X}$ direction is similar. While phonon dispersion can predict structural stability in the harmonic region, it cannot determine whether or not the structure collapses at a finite temperature. To evaluate the thermodynamic stability of the new CaP_3 structure, we perform canonical molecular dynamics (MD) simulations at a high temperature, 500 K . Figure 4(b) presents the fluctuations of the total potential energy for the 7 ps MD simulations and the final snapshot of the structure. Our results show that the CaP_3

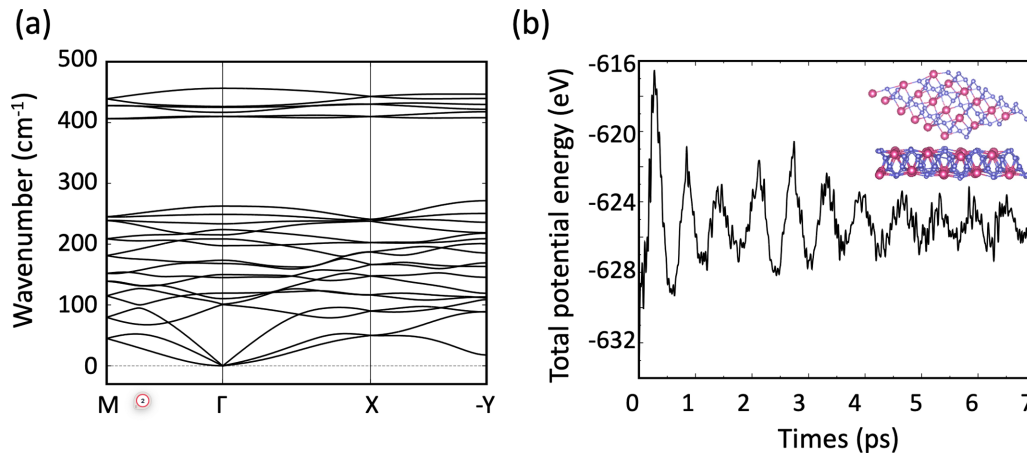


FIG. 4. The stability of CaP_3 . (a) Phonon band structures along the high-symmetry points are shown in Fig. 2(b). Total potential energy as a function of time during canonical MD simulations at 500 K with the final structural at the end of the simulation time of 7 ps (inset).

structure fluctuates relative to the $P2/c$ structure at 500 K, but is thermodynamically stable as the structure does not break or transition to another phase. The structure of the MD results from 3 ps to 7 ps, which reached thermal equilibrium at 500 K, is ensemble averaged over the MD time, showing that the Dirac state is perfectly preserved (see Supplemental Material [41]).

IV. CONCLUSION

We use an evolution algorithm in combination with first-principles density-functional theory calculations and find a new Dirac semimetal 2D CaP_3 , composed of light elements. The most intriguing feature of the new phase is that a nonsymmorphic and inversion symmetry guarantees symmetry-protected degeneracies in the electronic band structures, including a fourfold degenerate Dirac state that is intact under small strains. The Dirac state near the Fermi level is a result of satisfying the $4n + 2$ electron filling criterion with the location of the Dirac state controlled by strains. The

kinetic and thermodynamic stability of the new phase is confirmed by phonon dispersion analysis and MD simulations.

ACKNOWLEDGMENTS

This work was supported by the U.S. Department of Energy, Office of Science, Basic Energy Sciences, Materials Sciences and Engineering Division (W.L., S.Y., Y.Z., and M.Y.) and by the U.S. Department of Energy, Office of Science, National Quantum Information Science Research Centers, Quantum Science Center (QSC). S.-H.K. was funded by QSC for DFT band structure calculations and analysis. This research used resources of the Oak Ridge Leadership Computing Facility at the Oak Ridge National Laboratory, which is supported by the Office of Science of the U.S. Department of Energy under Contract No. DE-AC05-00OR22725 and resources of the National Energy Research Scientific Computing Center (NERSC), a U.S. Department of Energy Office of Science User Facility located at Lawrence Berkeley National Laboratory, operated under Contract No. DE-AC02-05CH11231 using NERSC award BES-ERCAP0024568.

- [1] L. Fu, *Phys. Rev. Lett.* **106**, 106802 (2011).
- [2] A. H. Castro Neto, F. Guinea, N. M. R. Peres, K. S. Novoselov, and A. K. Geim, *Rev. Mod. Phys.* **81**, 109 (2009).
- [3] F. D. M. Haldane, *Phys. Rev. Lett.* **61**, 2015 (1988).
- [4] C. L. Kane and E. J. Mele, *Phys. Rev. Lett.* **95**, 146802 (2005).
- [5] C. L. Kane and E. J. Mele, *Phys. Rev. Lett.* **95**, 226801 (2005).
- [6] S. Cahangirov, M. Topsakal, E. Aktürk, H. Sahin, and S. Ciraci, *Phys. Rev. Lett.* **102**, 236804 (2009).
- [7] C.-C. Liu, W. Feng, and Y. Yao, *Phys. Rev. Lett.* **107**, 076802 (2011).
- [8] G. Liu, S. Liu, B. Xu, C. Ouyang, H. Song, S. Guan, and S. Yang, *J. Phys. Chem. Lett.* **6**, 4936 (2015).
- [9] D. Malko, C. Neiss, F. Vines, and A. Görling, *Phys. Rev. Lett.* **108**, 086804 (2012).
- [10] L. Xu, R. Wang, M. Miao, X. Wei, Y. Chen, H. Yan, W. Lau, L. Liu, and Y. Ma, *Nanoscale* **6**, 1113 (2014).
- [11] X.-F. Zhou, X. Dong, A. R. Oganov, Q. Zhu, Y. Tian, and H.-T. Wang, *Phys. Rev. Lett.* **112**, 085502 (2014).
- [12] F. Ma, Y. Jiao, G. Gao, Y. Gu, A. Bilic, Z. Chen, and A. Du, *Nano Lett.* **16**, 3022 (2016).
- [13] Y. Jiao, F. Ma, J. Bell, A. Bilic, and A. Du, *Angew. Chem.* **128**, 10448 (2016).
- [14] B. Feng, O. Sugino, R.-Y. Liu, J. Zhang, R. Yukawa, M. Kawamura, T. Iimori, H. Kim, Y. Hasegawa, H. Li, L. Chen, K. Wu, H. Kumigashira, F. Komori, T.-C. Chiang, S. Meng, and I. Matsuda, *Phys. Rev. Lett.* **118**, 096401 (2017).
- [15] J. Kim, S. Baik, S. Ryu, Y. Sohn, S. Park, B. Park, J. Denlinger, Y. Yi, H. Choi, and K. Kim, *Science* **349**, 723 (2015).

- [16] Y. Lu, D. Zhou, G. Chang, S. Guan, W. Chen, Y. Jiang, J. Jiang, X. Wang, S. Yang, Y. Feng, Y. Kawazoe, and H. Lin, *npj Comput. Mater.* **2**, 16011 (2016).
- [17] S.-H. Kang, J. Park, S. Woo, and Y.-K. Kwon, *Phys. Chem. Chem. Phys.* **21**, 24026 (2019).
- [18] X. Sheng and B. Nikolic, *Phys. Rev. B* **95**, 201402(R) (2017).
- [19] S. Guan, Y. Liu, Z.-M. Yu, S.-S. Wang, Y. Yao, and S. A. Yang, *Phys. Rev. Mater.* **1**, 054003 (2017).
- [20] L. Zhongfei, W. Peihong, C. Qiaoyu, Y. Guang, J. Shaowei, and X. Kuangwei, *RSC Adv.* **9**, 2740 (2019).
- [21] G. Deping, G. Pengjie, T. Shiliang, F. Min, C. Limin, L. Zhengxin, L. Kai, L. Zhong-Yi, and J. Wei, *Sci. Bull.* **67**, 1954 (2022).
- [22] S. M. Young and C. L. Kane, *Phys. Rev. Lett.* **115**, 126803 (2015).
- [23] B. J. Wieder and C. L. Kane, *Phys. Rev. B* **94**, 155108 (2016).
- [24] A. K. Singh and R. G. Hennig, *Appl. Phys. Lett.* **105**, 042103 (2014).
- [25] V. M. Pereira and A. H. Castro Neto, *Phys. Rev. Lett.* **103**, 046801 (2009).
- [26] L. S. Panchokarla, K. S. Subrahmanyam, S. K. Saha, A. Govindaraj, H. R. Krishnamurthy, U. V. Waghmare, and C. N. R. Rao, *Adv. Mater.* **21**, 4726 (2009).
- [27] N. Lu, Z. Zhuo, H. Guo, P. Wu, W. Fa, X. Wu, and X. Zeng, *J. Phys. Chem. Lett.* **9**, 1728 (2018).
- [28] X.-L. Zhu, P.-F. Liu, Y.-Y. Wu, P. Zhang, G. Xie, and B.-T. Wang, *Mater. Adv.* **1**, 3322 (2020).
- [29] Z. Li, M. Qian, Z. H., D. Zhang, B. Chen, H. Qiu, and T. Zhang, *Mater. Today Commun.* **23**, 100925 (2020).
- [30] Y. Wang, J. Lv, L. Zhu, and Y. Ma, *Phys. Rev. B* **82**, 094116 (2010).
- [31] W. Luo, Y. Nakamura, J. Park, and M. Yoon, *npj Comput. Mater.* **7**, 2 (2021).
- [32] V. Blum, R. Gehrke, F. Hanke, P. Havu, V. Havu, X. Ren, K. Reuter, and M. Scheffler, *Comput. Phys. Commun.* **180**, 2175 (2009).
- [33] W. Huhn, B. Lange, V.-z. Yu, M. Yoon, and V. Blum, *Comput. Phys. Commun.* **254**, 107314 (2020).
- [34] V.-z. Yu, J. Moussa, P. Küs, A. Marek, P. Messmer, M. Yoon, H. Lederer, and V. Blum, *Comput. Phys. Commun.* **262**, 107808 (2021).
- [35] J. P. Perdew, K. Burke, and M. Ernzerhof, *Phys. Rev. Lett.* **77**, 3865 (1996).
- [36] J. Nocedal and S. Wright, *Numerical Optimization* (Springer, New York, 2006).
- [37] G. Kresse and J. Furthmüller, *Phys. Rev. B* **54**, 11169 (1996).
- [38] G. Kresse and J. Furthmüller, *Comput. Mater. Sci.* **6**, 15 (1996).
- [39] P. E. Blöchl, *Phys. Rev. B* **50**, 17953 (1994).
- [40] A. Togo and I. Tanaka, *Scr. Mater.* **108**, 1 (2015).
- [41] See Supplemental Material at <http://link.aps.org/supplemental/10.1103/PhysRevMaterials.7.124202> for the atomic structures and band structures of the new CaP₃ with $P\bar{1}$ and $C2$; calculated lattice parameter, atomic coordinates, and band structures for topological CaP₃ with $P2/c$ symmetry; Atomic and band structures of BaP₃ and SrP₃; The unfolded band structure of an ensemble average of 3 ps to 7 ps of atomic structures that have reached thermal equilibrium at 500 K.